

Comparison of amorphous silicon absorber materials: Light-induced degradation and solar cell efficiency

M. Stuckelberger, M. Despeisse, G. Bugnon, J.-W. Schüttauf, F.-J. Haug, and C. Ballif

Citation: [Journal of Applied Physics](#) **114**, 154509 (2013); doi: 10.1063/1.4824813

View online: <http://dx.doi.org/10.1063/1.4824813>

View Table of Contents: <http://scitation.aip.org/content/aip/journal/jap/114/15?ver=pdfcov>

Published by the [AIP Publishing](#)

Advertisement:



Re-register for Table of Content Alerts

Create a profile.



Sign up today!



Comparison of amorphous silicon absorber materials: Light-induced degradation and solar cell efficiency

M. Stuckelberger,^{a)} M. Despeisse, G. Bugnon, J.-W. Schüttauf, F.-J. Haug, and C. Ballif
*Ecole Polytechnique Fédérale de Lausanne (EPFL), Photovoltaics and Thin-Film Electronics Laboratory,
 Rue de la Maladière 71B, CH-2000 Neuchâtel, Switzerland*

(Received 18 August 2013; accepted 25 September 2013; published online 16 October 2013)

Several amorphous silicon (*a*-Si:H) deposition conditions have been reported to produce films that degrade least under light soaking when incorporated into *a*-Si:H solar cells. However, a systematic comparison of these *a*-Si:H materials has never been presented. In the present study, different plasma-enhanced chemical vapor deposition conditions, yielding standard low-pressure VHF *a*-Si:H, protocrystalline, polymorphous, and high-pressure RF *a*-Si:H materials, are compared with respect to their optical properties and their behavior when incorporated into single-junction solar cells. A wide deposition parameter space has been explored in the same deposition system varying hydrogen dilution, deposition pressure, temperature, frequency, and power. From the physics of layer growth, to layer properties, to solar cell performance and light-induced degradation, a consistent picture of *a*-Si:H materials that are currently used for *a*-Si:H solar cells emerges. The applications of these materials in single-junction, tandem, and triple-junction solar cells are discussed, as well as their deposition compatibility with rough substrates, taking into account aspects of voltage, current, and charge collection. In sum, this contributes to answering the question, “Which material is best for which type of solar cell?” © 2013 AIP Publishing LLC. [<http://dx.doi.org/10.1063/1.4824813>]

I. INTRODUCTION

Since the discovery of the Staebler-Wronski effect in 1977,¹ light-induced degradation of hydrogenated amorphous silicon (*a*-Si:H) has been widely discussed in the literature. Nevertheless, the processes that lead to (partially reversible) deteriorated conductivity and enhanced recombination in solar cells are not yet fully understood at the atomic and energy-band levels. Thus, light-induced degradation remains an active field of research for *a*-Si:H solar cells. Several models exist that explain aspects of light-induced degradation, see, e.g., the review article.² Recently, the role of vacancies and voids in light-induced degradation has received increased attention.^{3–5}

Leading institutes in the development of *a*-Si:H solar cells have claimed different plasma-enhanced chemical vapor deposition (PECVD) conditions for *a*-Si:H absorber materials to be best suited for high-efficiency solar cells showing high efficiency (with low light-induced degradation). These material classes include:

- Low-pressure VHF *a*-Si:H: Deposited at low pressure and very high frequency (VHF) (typically 0.2–0.8 mbar, 40–140 MHz) with rather low hydrogen dilution, these materials have small bandgaps and provide high currents, mainly for use in single-junction or micromorph tandem solar cells.^{6,7}
- Protocrystalline silicon (*pc*-Si:H): Deposited at moderate pressure and radio frequency (RF, 13.56 MHz) with a

hydrogen dilution close to the transition from *a*-Si:H to microcrystalline silicon (*μc*-Si:H), these materials have a wide bandgap for triple-junction solar cells. If grown thick enough, this material can turn into *μc*-Si:H with increasing crystallinity.^{8–10}

- Polymorphous silicon (*pm*-Si:H): The deposition conditions of *pm*-Si:H are close to those of *pc*-Si:H, but possibly a slightly higher pressure is used. In contrast to *pc*-Si:H, this material can be grown thick without a transition to *μc*-Si:H. Small crystallites, produced in the plasma phase, can be distributed homogeneously throughout the thickness as these deposition conditions are close to the powder regime.^{11,12}
- High-pressure RF *a*-Si:H: These materials are deposited at high pressures (typically above 6 mbar) and RF, often with a smaller inter-electrode gap.^{13,14}
- Triode: Deposition conditions similar to low pressure VHF *a*-Si:H but with an additional biased mesh between the electrodes lead to very low deposition rate but dense material.^{15,16}

a-Si:H deposition techniques other than PECVD, such as sputtering,¹⁷ hot-wire deposition,^{18,19} or expanded thermal plasma deposition²⁰ did not lead to high solar cell efficiencies or were not commercially practical, and will not be discussed here further.

In this contribution, we present a systematic study of different deposition conditions in order to sweep through the range of *a*-Si:H materials listed above. We restricted our study to PECVD with two electrodes, and only silane and hydrogen were used as gaseous precursors. We varied the hydrogen dilution, pressure, power, and excitation frequency

^{a)}Electronic mail: michael.stuckelberger@epfl.ch

of the plasma during the deposition of *a*-Si:H films incorporated as the absorber in single junction solar cells.

II. EXPERIMENTAL

A. Deposition conditions for intrinsic *a*-Si:H

All silicon layers were deposited by PECVD in an Octopus I cluster tool developed by INDEOtec SA,²¹ which allowed a wide variety of deposition conditions and fast equilibration times thanks to a closed reactor design.²²

The symmetric electrodes in each chamber were $15 \times 16 \text{ cm}^2$, the inter-electrode gap was 15 mm, and the excitation frequency was 13.56 MHz fixed or adjustable (VHF). Dedicated chambers were used for *p*-layer, *n*-layer, and *i*-layer depositions, and different chambers were used for *i*-layers deposited at RF and VHF.

Table I summarizes the deposition parameters of the four plasma regimes investigated in this study. For each of these regimes, the hydrogen dilution was widely varied while keeping the total gas flow constant. Exceptions for very high or low dilutions were made due to limitations of the mass flow controllers. Note that the power was measured at the generator output.

The deposition temperature was kept at 200 °C. For the best bulk material quality in the different pressure regimes, we chose the lowest power density that allowed plasma ignition for all hydrogen dilutions. Temperature and power series for selected deposition conditions complete the explored parameter space.

B. Solar cell design

The *a*-Si:H films described in Sec. II A were incorporated into solar cells. We used the same cell design (see Fig. 1) for all experiments and changed only the intrinsic bulk layer to obtain a direct comparison of bulk layer properties resulting from the investigated deposition conditions.

The *a*-Si:H solar cells were deposited in the superstrate configuration (*p-i-n*) on 0.5 mm thick Schott AF 32 glass substrates. For the front and back contacts, 2 μm thick boron-doped ZnO (ZnO:B) was deposited by low-pressure chemical vapor deposition (LPCVD). All solar cells were co-deposited on four different substrates with varying roughness: Three substrates consisted of co-deposited ZnO:B on glass. On one, as-deposited ZnO:B was used; on two others, the ZnO:B was treated for 4 and 10 min with an argon plasma to smoothen the surface texture from V- into U-shaped. This leads to not only less shunting but also less light scattering.²³ All results shown below except in

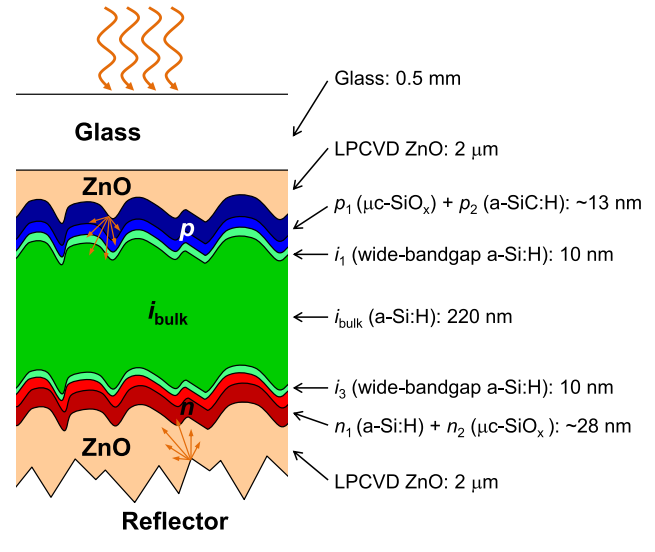


FIG. 1. Solar cell structure used for all *p-i-n* solar cells.

Sec. III F refer only to the substrate treated for 4 min. The presented trends, however, were consistent across all substrates. As a flat reference, a fourth substrate with smoothly grown LPCVD ZnO:B was used, also treated for 4 min with an argon plasma.^{24,25}

Solar cell deposition began with a *p*-type bilayer. Directly on the ZnO, we deposited a microcrystalline silicon-oxide layer (*p*-($\mu\text{c-SiO:H}$)) for good electrical contact, enhanced transparency, and shunt-quenching.^{26,27} This was followed by an amorphous silicon carbide layer (*p*-(*a*-SiC:H)) with a wide bandgap to provide a high electric field. The *p*-type layers were deposited at nominally 150 °C and 40.68 MHz.

In order to keep the sensitive *p-i* and *i-n* interfaces as similar as possible from one deposition to the other, we sandwiched the 220 nm thick intrinsic bulk absorber layer under investigation between 10 nm thick intrinsic *a*-Si:H buffer layers at both interfaces, deposited at 200 °C, RF, and high hydrogen dilution. These buffer layers (as well as the doped layers and ZnO contacts) were the same on all solar cells, regardless of the intrinsic bulk layer. The deposition conditions were chosen right at the transition from *a*-Si:H to $\mu\text{c-Si:H}$ but still amorphous enough that the buffer layer grew amorphous even on $\mu\text{c-Si:H}$.

The three *i*-layer depositions were followed by an *n*-type bilayer consisting of an amorphous silicon layer (*n*-(*a*-Si:H)) and a microcrystalline silicon oxide layer (*n*-($\mu\text{c-SiO:H}$)) in contact with the back ZnO:B. They were deposited at 200 °C and 40.68 MHz.

In addition to SiH₄ and H₂, CO₂ was used for oxide layers, B(CH₃)₃ for *p*-type layers, PH₃ for *n*-type layers, and CH₄ for the carbide layer. For better reproducibility and to ensure that cell performance was not limited by the doped layers, all doped layers were thicker than those in cells optimized for high efficiency.

For each substrate, an array of 16 cells, each 0.25 cm² in size, was defined and polytetrafluoroethylene (PTFE) was used as a white back reflector.

TABLE I. Deposition conditions for intrinsic bulk *a*-Si:H layers.

Pressure (mbar)	Power (W)	Total gas flow (sccm)	Frequency (MHz)
0.2	3	30	40.68
2.5	3	85	13.56
5.0	10	100	13.56
9.0	20	100	13.56

C. Layer and cell characterization

For measurements of intrinsic bulk layer properties, the layers were deposited on 0.5 mm thick Schott AF 32 glass substrates and 250 μm thick double-side polished intrinsic (100) crystalline silicon (*c*-Si) wafers.

Ellipsometry measurements were performed using a UVISEL ellipsometer from Horiba Jobin Yvon (with monochromators for IR and UV/Vis) between 0.6 and 6 eV, and transmission measurements using a Lambda 900 spectrometer from Perkin Elmer between 300 and 2000 nm. For Fourier transform infrared (FTIR) spectroscopy measurements, a Spectrum 2000 spectrometer from Perkin Elmer and a Nicolet 8700 spectrometer from Thermo Scientific were used. Raman crystallinity was measured on an Invia Raman microscope from Renishaw and on a Senterra Raman microscope from Bruker with green lasers.

Current-voltage (I-V) characteristics were measured with a four-lamp solar simulator from Wacom (class AAA) under standard conditions (AM1.5g, 1000 W m^{-2} , 25 $^{\circ}\text{C}$),^{28,29} current was determined from an external quantum efficiency (EQE) system built in-house. Light soaking was performed in a sun simulator from Solaronix (class AAA) under standard conditions (AM1.5g, 1000 W m^{-2} , 50 $^{\circ}\text{C}$).³⁰

III. RESULTS AND DISCUSSION

A. Plasma regimes

Figure 2 shows the lowest power for pure silane and hydrogen plasmas (both for RF and VHF) for which a stable plasma could be sustained. Instead of the breakdown voltage that is more commonly shown for Paschen curves,³¹ we show here the extinction power as it is more relevant for the deposition of layers. This graph gives an overview of the characteristics of our reactor and the deposition conditions that are accessible. The curves for RF are less smooth than those for VHF because of the amplifier precision limit of 1 W. In further discussion, we refer to the “turning point”³² as the lowest pressure at which the plasma could be sustained, and to the “diffusion/drift” branch as the part of a Paschen curve at pressures significantly above the pressure of minimum extinction power.

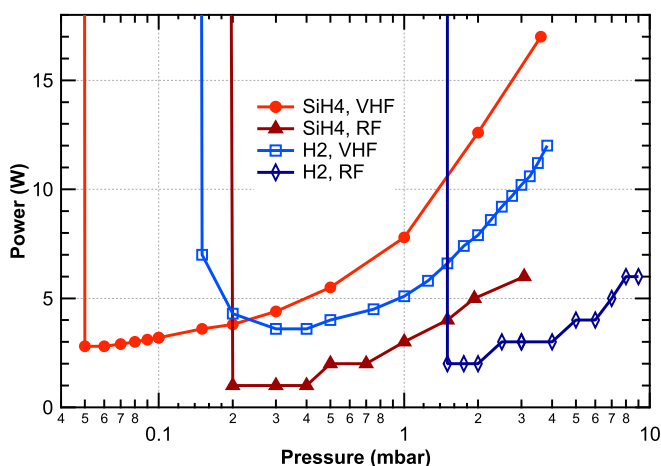


FIG. 2. Plasma extinction power as a function of gas pressure for pure H_2 and SiH_4 plasmas powered at RF and VHF.

Four observations are relevant for *a*-Si:H deposition from silane/hydrogen plasma by PECVD:

- (i) At high pressures, higher power is needed when the frequency is increased from 13.56 to 40.68 MHz.
- (ii) At high pressures, higher power is needed for SiH_4 than for H_2 .
- (iii) VHF sustains plasmas at much lower pressures than RF.
- (iv) SiH_4 plasmas can be sustained at lower pressures than H_2 plasmas.

Assuming vanishing electron concentrations close to the electrodes, the extinction power at high pressures is limited by the ionization rate ν_i of gas molecules via electron impact^{33,34}

$$\nu_i = \alpha + \beta \cdot (L - 2A)^{-2}. \quad (1)$$

Here, α and β are constants that include the reactor size and electron diffusion coefficients, L denotes the inter-electrode gap and $A = V_{\text{dr}}/(2\pi f)$ is the electron displacement amplitude expressed in terms of the electron drift velocity V_{dr} and the RF field frequency f .

From Eq. (1), we see that an increase of the frequency leads to a lower electron displacement amplitude and a lower ionization rate. Hence, a stronger electric field may be needed for the electrons to acquire sufficient energy to perform electron-impact ionization of molecules, which may explain why a higher power is needed to sustain VHF plasmas, as observed in (i).

In contrast, Eq. (1) is not valid close to the turning point, where the mean free path of the electrons is of the same order as the inter-electrode distance, $L \approx 2A$, and electron loss at the electrodes limits the plasma-sustaining conditions. With increasing frequency (lower A), fewer electrons are lost at the electrodes and the plasma can be sustained at lower pressures; this explains (iii).

Similar reasoning explains (iv): A SiH_4 plasma can be operated at lower pressures compared to a H_2 plasma due to a higher dissociation cross section and hence lower mean free path of the electrons.

Observation (ii) has already been reported elsewhere.^{35,36} For a given pressure, more electrons are lost in collisions in a SiH_4 plasma than in a H_2 plasma; hence, a higher power is needed.

The differences between H_2 and SiH_4 plasmas and the crossing of their Paschen curves are of great importance for depositions at low power as is desired for highly stable solar cells:

- (a) For low pressures, hydrogen dilution can make it impossible to sustain a plasma, while at high pressures it allows a plasma to be sustained at a lower power.
- (b) For low pressures, where electron loss at the electrodes dominates, ignition with an external electron source can reduce the ignition power dramatically. However, this has hardly any effect at higher pressures, where electron loss by collisions in the gas phase limits the plasma ignition. More concretely, the plasmas for the hydrogen dilution series at 0.2 mbar were ignited with

the help of an external electron source, while only slightly higher power but no external charges were required for the ignition of the plasmas in the dilution series at 2.5, 5.0, and 9.0 mbar.

B. Deposition rates

The deposition rates of the investigated plasma conditions are shown in Fig. 3. For each hydrogen dilution series (see Fig. 3(a)), one can distinguish two different branches: The deposition rate increases with increasing hydrogen dilution at low dilution, and seems to decrease logarithmically at high dilution.

At low hydrogen dilutions, powder formation with non-uniform deposition of the layer is observed. Hence, the deposition rate is lowered by polymerization of SiH₄ towards higher silanes that are pumped away and do not contribute to the growing film.

For the same reason, the hydrogen dilution with the highest deposition rate (indicated with black circles in Fig. 3(a)) increases with pressure; this is also the case if the power is kept the same for all pressures (results not shown here). The collisions of the film precursors in the plasma phase increase with increasing pressure; hence, more powder is produced and fewer film precursors reach the surface to contribute to layer growth.

The decrease of the deposition rate for high hydrogen dilutions is not intuitive: One might think that increasing the dilution (by decreasing the SiH₄ flow while keeping the total flow constant) would limit the deposition rate because of the low SiH₄ flow (that would lead to highly depleted plasma conditions). However, this explanation can be excluded for our situation. A simple estimation of the maximum deposition rate³⁷

$$r_{\max} = 0.0962 \frac{\Phi_{\text{SiH}_4}}{S} \left(\frac{\text{m}^2 \cdot \text{\AA}}{\text{sccm} \cdot \text{s}} \right), \quad (2)$$

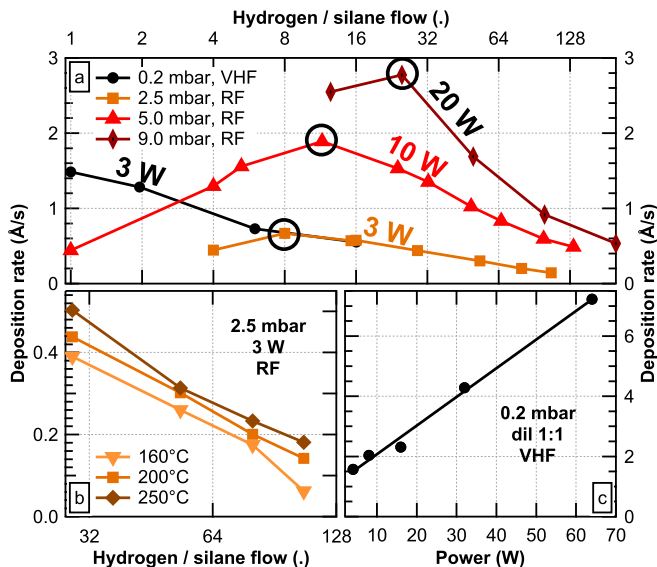


FIG. 3. Deposition rate as a function of H₂:SiH₄ flow ratio for different pressures (a: 200 °C) and temperatures (b: 2.5 mbar, 3 W, RF) and as a function of power (c: 0.2 mbar, VHF, H₂:SiH₄ flow ratio of 1:1) with a linear fit.

with Φ_{SiH_4} the silane flow and S the inner chamber surface, predicts at least twice the measured deposition rate, even for the most diluted deposition conditions.

We suggest another mechanism for the deposition rate decrease with hydrogen dilution based on a diminishing fraction of the power being used to dissociate SiH₄ compared to that used for H₂ dissociation, where the latter does not directly contribute to layer growth. First, we define the partial power available for silane dissociation

$$P_{\text{SiH}_4} \doteq P \cdot \frac{\Phi_{\text{SiH}_4}}{\Phi_{\text{SiH}_4} + \Phi_{\text{H}_2}}. \quad (3)$$

Here, P is the total power, and the silane and hydrogen flow rates are given by Φ_{SiH_4} and Φ_{H_2} , respectively. For the investigated deposition conditions, the deposition rate r should be proportional to the concentration c_{SiH_3} of the main film precursor in the plasma, SiH₃, which in turn depends on N_{e3} , the number of electrons³⁸ with a sufficiently high energy to initiate the SiH₄ → SiH₃ + H reaction. The electron impact energy needed for this reaction path (8.75 eV)³⁹ is close to the dissociation energy of molecular hydrogen (8.85 eV).⁴⁰ Thus, the number of electrons used for silane dissociation is proportional to $N_{e3} \cdot \frac{\Phi_{\text{SiH}_4}}{\Phi_{\text{SiH}_4} + \Phi_{\text{H}_2}}$ and we conclude that

$$r \propto c_{\text{SiH}_3} \propto N_{e3} \cdot \frac{\Phi_{\text{SiH}_4}}{\Phi_{\text{SiH}_4} + \Phi_{\text{H}_2}} \propto P \cdot \frac{\Phi_{\text{SiH}_4}}{\Phi_{\text{SiH}_4} + \Phi_{\text{H}_2}} \doteq P_{\text{SiH}_4}. \quad (4)$$

The deposition rate as a function of the partial power is plotted in Fig. 4. Indeed, we see that the deposition rate increases linearly with the partial power for low P_{SiH_4} . Note that the curves for different pressures and powers overlap well within experimental error. The proportionality constant measured here is on the order of 5 Å W⁻¹ s⁻¹ or, considering only one electrode surface, 1200 Å cm² W⁻¹ s⁻¹. This value allows us to estimate the maximum deposition rate for a given inter-electrode distance with RF power. For VHF, the deposition rate increases linearly with P_{SiH_4} too, however, with a lower slope. For higher partial powers, the deposition rate stays below the linear behavior due to increasing utilization of SiH₄ for species that are not deposited, e.g., powder.

The temperature dependence of the deposition rate is weak as can be seen in Fig. 3(b). However, it was systematically observed for different pressures and dilutions that the deposition rate increases with increasing temperature, in agreement with measurements by Andújar *et al.*⁴¹ (For the triode reactor configuration, where we expect the temperature dependence of the deposition rate to be similar to that in diode configuration, such a temperature dependence was not seen within the temperature range of interest.^{15,42}) We suggest the following explanation: With increasing temperature, the desorption rate of hydrogen from the surface is higher, and hence less hydrogen is available at the surface. At the same time, more dangling bonds provide “sticking places” for film precursors, thus leading to a higher deposition rate. One may imagine that powder formation could also be responsible: There tends to be less powder at higher temperatures;⁴³ therefore, the deposition rate could be higher because fewer film precursors are lost to powder. Further,

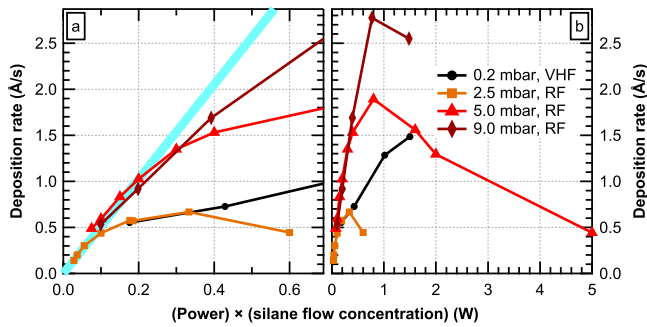


FIG. 4. Deposition rate as a function of the partial power $P_{\text{SiH}_4} = \text{power} \times \text{silane flow concentration}$. (a) shows the same data as (b) but with low silane partial powers magnified.

following the ideal gas law, a higher temperature means a lower gas number density, and hence fewer gas-phase collisions and less powder. However, no powder formation was observed for the layers presented in Fig. 3(b) or for other series in which this temperature dependence was observed. Therefore, we conclude that powder formation does not play a major role in the deposition rate increase with temperature.

In Fig. 3(c), we see that the deposition rate increases linearly with power for depositions at VHF, 0.2 mbar, and a H_2 : SiH_4 flow ratio of 1:1. This confirms that the deposition rate is indeed limited by silane dissociation.

C. Bandgap

Optical layer characterization was performed by combined fitting of three-angle ellipsometry measurements and transmission measurements of layers deposited on glass with a Tauc-Lorentz model,⁴⁴ taking into account surface roughness. The bandgaps—parametrized here by the model-independent energy E_{04} , at which the absorption coefficient reaches 10^4 cm^{-1} —of the dilution series for different pressures are shown in Fig. 5. Other bandgap parametrizations like the Tauc-Lorentz bandgap E_g^{TL} or the Tauc bandgap E_g^{T} —all determined from fits to ellipsometry and

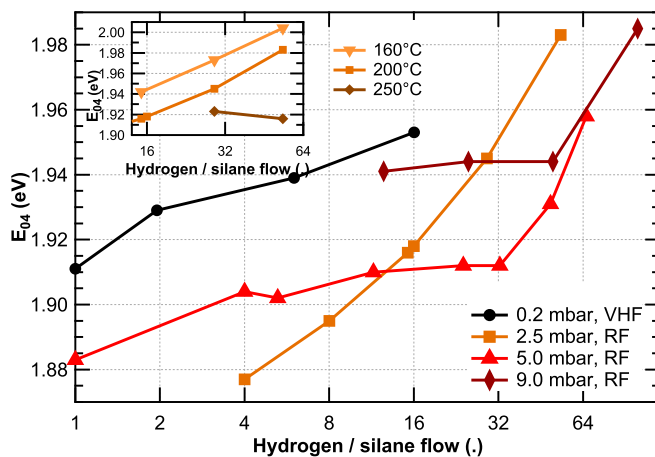


FIG. 5. Energy E_{04} , where the absorption coefficient reaches 10^4 cm^{-1} , for different hydrogen dilutions and deposition conditions. The inset shows the temperature and hydrogen dilution dependence of E_{04} for layers deposited at RF, 2.5 mbar.

transmission data—show the same trends. For higher hydrogen dilutions than those shown here, Raman measurements showed a crystalline peak at around 520 cm^{-1} ; in these cases, the fitting of the ellipsometry/transmission data with a single Tauc-Lorentz oscillator was no longer adequate and the measurements are not shown here. Thus, the data at the highest hydrogen dilution mark the transition from $a\text{-Si:H}$ to $\mu\text{c-Si:H}$. Note that the hydrogen dilution at which the transition takes place increases with increasing pressure due to decreased ion bombardment on the surface and hence a lower surface mobility of the adatoms.⁴⁵

As reported elsewhere,^{46–48} the bandgap increases with increasing hydrogen dilution—moderately at low dilutions and stronger close to the transition. Whether this is due to a depletion of states close to the valence band,⁴⁶ to decreased structural disorder,⁴⁷ to compressive stress associated with hydrogen incorporation in divacancies and nanosized voids,⁴⁸ or to a combination of these effects is not clear.

D. Solar cell performance after light soaking

The solar cell results reported in this section are taken from the cell on each substrate with the highest $V_{\text{oc}} \times FF$ product in the initial state (with V_{oc} the open circuit voltage and FF the fill factor). These cells are most often also the best on their respective substrate after light soaking.

Differences among various absorber layers are often visible only after light soaking, when the conversion efficiency is typically limited by electron/hole recombination at light-induced defects. Therefore, initial solar cell performance is not shown here, and we instead concentrate on solar cell performance after light soaking and the relative light-induced degradation.

The performance of solar cells (in terms of V_{oc} , FF , short-circuit current density J_{sc} , and conversion efficiency) with the i -layers that have been discussed in Secs. III A–III C is shown in Fig. 6. As expected from the layer properties of the bulk absorber material, V_{oc} increases generally with hydrogen dilution due to a bandgap increase (see Fig. 6(a)), until it drops sharply as soon as nanocrystals start to grow near the i - n interface at the transition to $\mu\text{c-Si:H}$. The highest V_{oc} that can be obtained by varying the hydrogen dilution for a given pressure increases with pressure (emphasized with black circles in Fig. 6(a)). This can be partially explained by the increased bandgap of the corresponding layers as shown in Fig. 5. In addition, the decreased ion bombardment of the underlying p - and buffer layers at the beginning of the i -layer deposition could create fewer defects at the p - i interface.

In Fig. 6(c) we see that the increased bandgap with dilution leads to a decreased current due to less absorption of low-energy photons, consistent with Figs. 5 and 6(a). At very high dilutions, where crystallites start to grow near the i - n interface, the current drops quickly due to poor collection of charge carriers that are excited in the crystalline phase (too high barrier for holes at the crystalline/amorphous interface). However, these charge carriers generated from photons at wavelengths above 750 nm are collected in quantum efficiency measurements under reverse-bias voltage.

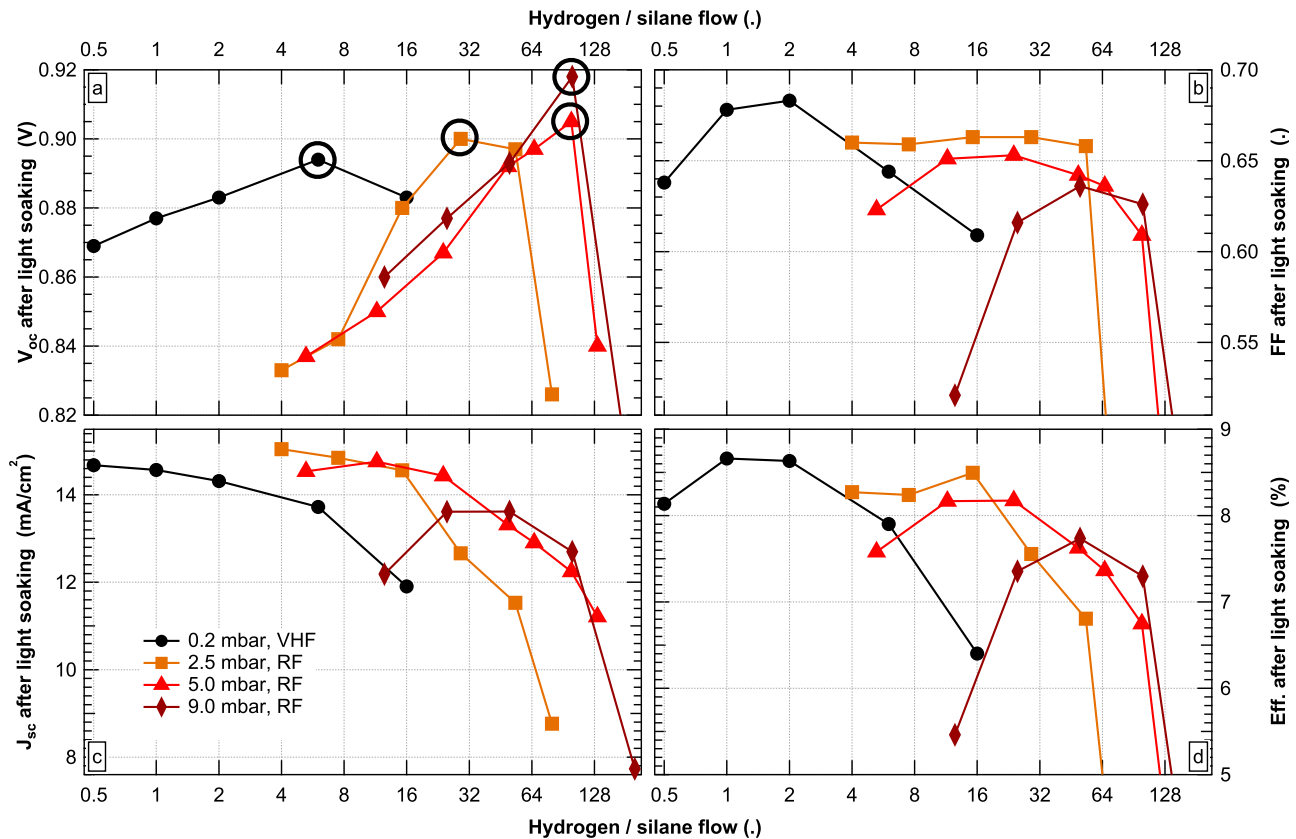


FIG. 6. Performance of *a*-Si:H solar cells (a: V_{oc} , b: FF , c: J_{sc} , d: efficiency), deposited at different pressures and hydrogen dilutions, after 1000 h of light soaking under AM1.5g light (1000 W cm^{-2}) at 50°C . All absorber layers of these solar cells were deposited at 200°C .

For the combination of very low hydrogen dilutions and high pressures, the current is lower than expected from the bandgap of the absorber layers. The difference between external quantum efficiency measurements performed under -1 V bias voltage ($\text{EQE}(-1 \text{ V})$) and without any bias voltage ($\text{EQE}(0 \text{ V})$) shows that in these cases there is a large collection problem over the entire absorption spectrum but it is accentuated for blue light. Further, visual inspection of the corresponding layers and substrate holders showed powder deposition. These two observations support the hypothesis that *a*-Si:H deposited under these conditions contains many defects and is porous. The poor material quality resulting from high-pressure and low-hydrogen-dilution depositions affects the FF even more than the J_{sc} as we see to the left of the maximum (for low hydrogen dilutions) in Fig. 6(b).

Note another aspect: The maximum FF obtained for a given series decreases with increasing pressure. This is in agreement with a generally lower current for high pressures that cannot be justified by the bandgap. Indeed, a comparison of the quantum efficiency with and without bias voltage reveals that there is a charge-collection problem that is wavelength independent, i.e., the relative difference between $\text{EQE}(-1 \text{ V})$ and $\text{EQE}(0 \text{ V})$ is constant for high-pressure depositions. However, the absorber material quality of the best cells deposited at 9.0 mbar does not seem to be worse than at lower pressures, as the relative light-induced degradation is similar (see the discussion in Sec. III E).

So, why does the maximum FF decrease with increasing pressure? The underlying reason is not clear, but we note

that it is not necessarily linked to the intrinsic bulk properties since the doped and buffer layers were developed for bulk absorbers deposited at low pressure. Consequently, there may be a bandgap mismatch or a difference in the amount of hydrogen incorporated at the *p-i* interface, *p*-layer etching, or similar interface problems that reduce the charge collection.

Figure 6(d) shows the conversion efficiencies of the solar cells calculated from the V_{oc} , J_{sc} , and FF values shown in Figs. 6(a)–6(c). It shows the trade-off between high voltage (wide-bandgap absorber), high current (small-bandgap absorber), and high FF (good charge collection). As the FF varies most for the different deposition conditions, trends in efficiency mainly reflect trends in FF , which turns out to be the most crucial parameter when optimizing solar cell efficiency.

In contrast to United Solar Systems Corp.'s successful industrial production of top cells for *n-i-p* triple junctions with wide-bandgap absorbers and good charge collection,⁹ it is questionable whether wide-bandgap absorber materials are well suited for high-efficiency solar cells in the *p-i-n* configuration. For *a*-Si:H single junction solar cells as well as for *a*-Si:H top cells in micromorph solar cells, the current that is needed in the *a*-Si:H cell for a high-efficiency solar cell cannot be obtained with a wide-bandgap absorber layer, as an increase of $V_{oc} \times FF$ can never compensate for the lower current. For top cells in triple-junctions, it is not clear whether a wide-bandgap top cell (higher $V_{oc} \times FF$ but lower current and thicker; hence stronger light-induced

degradation), or a small-bandgap top cell (lower $V_{oc} \times FF$ but higher current; can be made thinner and hence lower light-induced degradation), gives better performance. This depends on the quality of each layer and on the roughness of the used substrate (see discussion in Sec. III F).

Overall, it is important to note that with increasing pressure, the process window within which high-efficiency solar cells can be obtained gets smaller. Even hydrogen dilutions that are not very far away from the transition from a -Si:H to μ c-Si:H tend to lead to powdery plasmas and poor material quality.

Note that we did not optimize the doped layers for record efficiency, nor adapt them to different i -layer process pressures. Nevertheless, efficiencies above 7.5% were obtained for each processing pressure and the best cells without an antireflective coating reached a very high efficiency of 8.7% with a FF of 68% after light soaking.

E. Relative light-induced degradation

Figures 7(a) and 7(b) show the relative light-induced degradation of the FF

$$\Delta FF = \frac{FF_{\text{after light soaking}} - FF_{\text{before light soaking}}}{FF_{\text{before light soaking}}} \quad (5)$$

and of the conversion efficiency. Most trends observed in Fig. 6 are reproduced here, which reflects the fact that the i -layer quality governs the initial state less than the light-

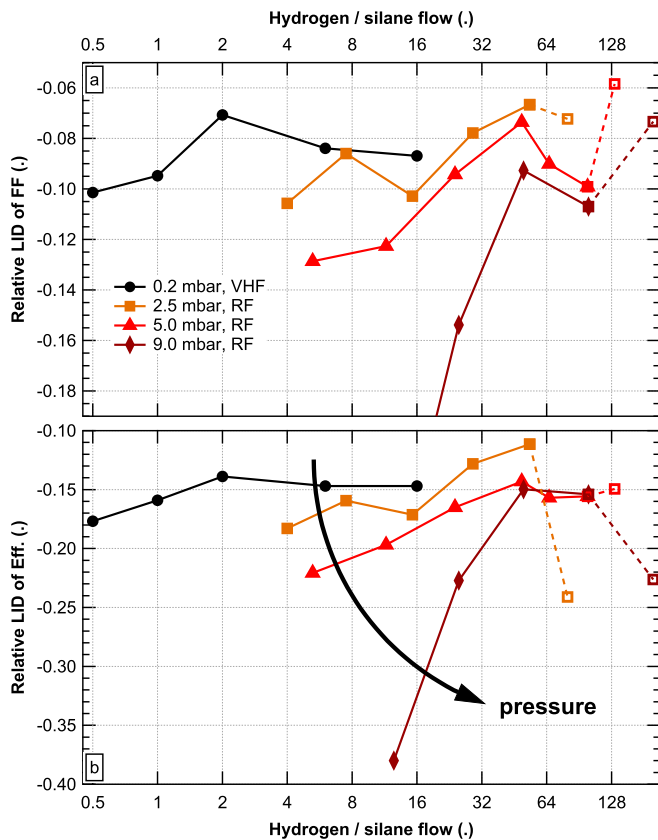


FIG. 7. Relative light-induced degradation of the FF (a) and conversion efficiency (b) for the cells in Fig. 6. Open symbols indicate cells with a non-zero μ c-Si:H fraction and hence different degradation mechanisms.

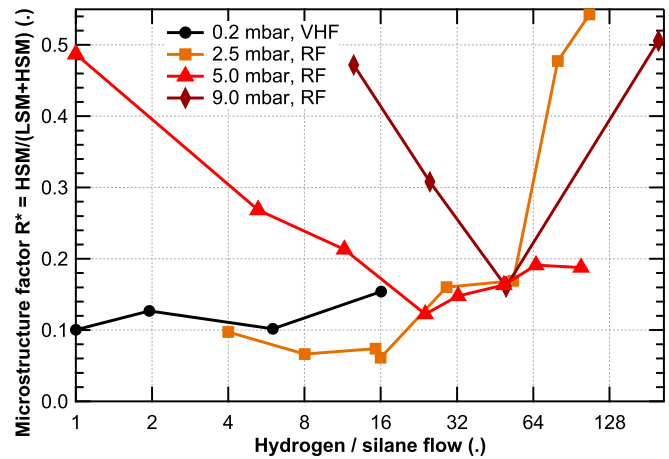


FIG. 8. Microstructure factor R^* of layers deposited under different pressures and with different hydrogen dilutions. The same deposition conditions have been used to deposit the bulk absorber layers of the solar cells discussed in Secs. III D and III E.

soaked state. Moreover, the FF is the parameter that dominates the efficiency after light soaking. We see that cells deposited under higher pressure degrade more, especially for low hydrogen dilutions. For lower pressures, there is a wider range of dilutions that provides low-degradation cells than for higher pressures. However, at all pressures there is an optimum hydrogen dilution for which the cells degrade only about 15%, which is remarkably low. These solar cell results are in accordance with the conclusions from plasma and layer analysis.

A correlation between light-induced degradation and the microstructure factor

$$R^* = \frac{HSM}{LSM + HSM}, \quad (6)$$

has been reported elsewhere,⁴⁹ where HSM and LSM are the integrals of the fits of the high and low hydrogen stretching modes around 2090 cm^{-1} and 2000 cm^{-1} , respectively.

For all layers investigated in the present article, the stretching mode absorption bands (hence R^*) have been measured by FTIR and fitted with two Gaussians after correction with a linear baseline. In all series except 0.2 mbar, R^* shows a minimum (see Fig. 8). The range of small R^* becomes narrower and more pronounced as the pressure is increased (note the logarithmic scale). The broad minimum of low R^* for low pressures is consistent with the series of Alpuim *et al.* at 100 mTorr.⁵⁰

In our case, the light-induced degradation of the cells follows the trends of R^* , as can be seen comparing Fig. 8 with Fig. 7. For low pressures, R^* does not depend much on the hydrogen dilution up to the transition to μ c-Si:H growth. In contrast, R^* strongly depends on the hydrogen dilution for higher pressures which can be attributed to the powdery deposition conditions that result in larger voids and more SiH_n bonds with $n \geq 2$.⁵¹

F. Substrate dependence of V_{oc}

Until now, the substrate dependence of cell parameters was not addressed because the discussed trends were

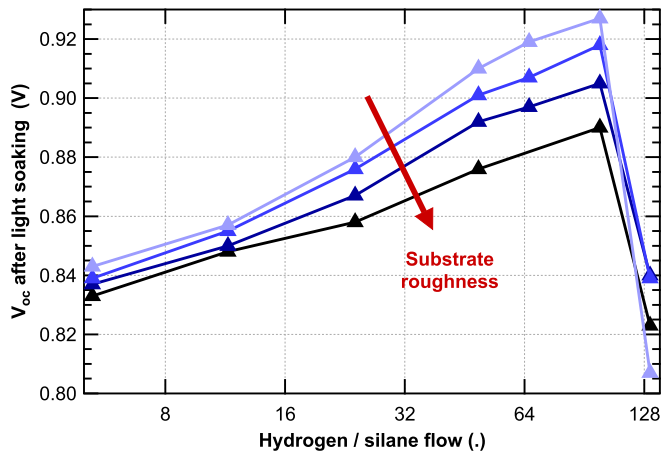


FIG. 9. V_{oc} after light soaking for the hydrogen dilution series of solar cells co-deposited on four substrates with different roughnesses.

observed for all substrates. Nevertheless, solar cell performance, and in particular V_{oc} , can depend strongly on the substrate roughness. In Fig. 9, V_{oc} is shown for cells co-deposited on four different substrates for the hydrogen dilution series deposited at 5.0 mbar. For all other hydrogen dilution series (variable pressure, deposition temperatures of 160 and 250 °C), the same trends were observed.

For low hydrogen dilutions, V_{oc} decreases only slightly with increasing roughness. At least two mechanisms can lead to this substrate dependence: First, the surface area of a rough substrate is larger than that of a smooth substrate, leading to thinner doped layers. Second, non-conformal or even non-homogeneous deposition on a rough substrate leads to a higher probability that the front and back electrode may be nearly touching or may be poorly covered by the doped and intrinsic layers. This can introduce weak diodes (parallel to the standard diode in an equivalent circuit) that lower V_{oc} on rough substrates, similar to porous zones in microcrystalline solar cells.²³

Higher hydrogen dilution increases the substrate dependence of V_{oc} dramatically from about 10 to 40 mV, and this cannot be explained in the same manner. To understand this substrate dependence, two solar cells were deposited right at the transition from *a*-Si:H (close to the *p-i* interface) to μ c-Si:H (close to *i-n* interface). The only difference between the cells was the *i*-layer thickness. Because of the thickness dependence of crystallinity near the transition, the *i*-layer was purely amorphous for the thinner cell (providing 950 mV V_{oc} after light soaking) but grew microcrystalline after a few hundred nanometers in the 1 μ m thick solar cell. A transmission electron microscope (TEM) image of the thick cell is shown in Fig. 10. It reveals substrate-dependent porous zones, seen as chains of voids located above peaks of the underlying ZnO texture and highlighted by arrows in the figure. These zones could create weak diodes similar to porous zones in μ c-Si:H and thus decrease V_{oc} . (Note that, in μ c-Si:H, porous zones are located above ZnO valleys.) Further investigations of these zones are ongoing.

While the increased dependence on substrate roughness for high hydrogen dilutions is less an issue for triple junctions, where one can use wide-bandgap *a*-Si:H materials

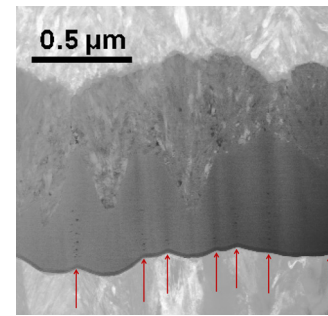


FIG. 10. TEM image of a 1 μ m thick solar cell with an *i*-layer deposited at the transition from *a*-Si:H to μ c-Si:H. Arrows indicate peaks of the ZnO substrate, above which chains of voids are located. TEM image taken by D. Alexander.

together with smoother substrates, one needs better light trapping for single-junction or micromorph tandem devices and hence rougher substrates. However, on rougher substrates, the bandgap increase (compared to lower hydrogen dilutions) is not fully reflected in the V_{oc} . The slightly increased V_{oc} does not compensate for the lower current, and thus wide-bandgap materials deposited at high dilution are not optimal for *a*-Si:H single-junction or micromorph tandem devices.

IV. CONCLUSIONS

Using VHF and RF PECVD, intrinsic *a*-Si:H layers were deposited in a single deposition system varying hydrogen dilution, pressure, temperature and power, covering low-pressure VHF *a*-Si:H, protocrystalline, polymorphous and high-pressure RF *a*-Si:H materials. This allowed for the first time a direct comparison of these materials regarding their optical properties and the performance of solar cells using them as absorber layers. The plasma physics was discussed to explain the differences observed.

While optimum hydrogen dilutions leading to relative light-induced degradation below 15% were identified for all process pressures, the process windows leading to such results narrow for increasing deposition pressure due to powdery plasmas at low dilutions. The best cells reach post-light-soaking efficiencies of 8.7% and *FF* of 68% without an antireflective coating.

Light-induced degradation was shown to correlate well with the microstructure factor R^* , which has a sharp minimum for high pressures but depends only little on the hydrogen dilution for lower pressures.

While the same trends were observed for cells co-deposited on four substrates with different roughnesses, their sensitivity changed considerably with the substrate roughness. In particular, the substrate dependence of V_{oc} increases dramatically from about 10 to 40 mV from low to high hydrogen dilutions (small to wide bandgap material). In a TEM image of a solar cell with a very wide-bandgap absorber, chains of small voids or porous zones were identified above peaks of the underlying ZnO. On rough substrates, these zones may create weak diodes that lead to a decrease of V_{oc} and limit the use of wide-bandgap materials to smooth substrates.

ACKNOWLEDGMENTS

We wish to acknowledge D. Alexander for performing the TEM measurement, M. Carlberg and L. Garcia for taking part of the current-voltage and EQE measurements, S. De Wolf and A. Howling for discussions, T. Matsui from PVTEC (Tsukuba, Japan) for allowing us to use their FTIR and Raman measurement setups, G. Choong from TEL solar (Neuchâtel, Switzerland) for providing us access to their Raman measurement setup, and INDEOtec for the PECVD reactor and technical support.

This work was supported in part by Competence Center Energy and Mobility, and Swisselectric Research (DURSOL project, www.dursol.ch), by the Swiss Federal Office of Energy under Grant SI/500750-01, and by the FP7 Project “Fast Track,” funded by the European Commission under Grant 283501.

- ¹D. L. Staebler and C. R. Wronski, “Reversible conductivity changes in discharge-produced amorphous Si,” *Appl. Phys. Lett.* **31**, 292–294 (1977).
- ²T. Shimizu, “Staebler-Wronski effect in hydrogenated amorphous silicon and related alloy films,” *Jpn. J. Appl. Phys., Part 1* **43**, 3257–3268 (2004).
- ³S. Zhang and H. Branz, “Hydrogen above saturation at silicon vacancies: H-pair reservoirs and metastability sites,” *Phys. Rev. Lett.* **87**, 105503 (2001).
- ⁴A. H. M. Smets, W. M. M. Kessels, and M. C. M. van de Sanden, “Vacancies and voids in hydrogenated amorphous silicon,” *Appl. Phys. Lett.* **82**, 1547–1549 (2003).
- ⁵A. Smets, C. Wronski, M. Zeman, and M. van de Sanden, “The Staebler-Wronski effect: New physical approaches and insights as a route to reveal its origin,” *Mater. Res. Soc. Symp. Proc.*, San Francisco, CA (Materials Research Society, 2010), Vol. 1245, p. 1245–A14-02.
- ⁶S. Benagli, D. Borrello, E. Vallat-Sauvain, J. Meier, U. Kroll, J. Hoetzel, J. Bailat, J. Steinhauser, M. Marmelo, G. Monteduro, and L. Castens, “High-efficiency amorphous silicon devices on LPCVD-ZnO TCO prepared in industrial KaiTM-M R&D reactor,” in *24th EU PVSEC Proceedings*, Hamburg, Germany (WIP Wirtschaft und Infrastruktur GmbH & Co Planungs-KG, 2009), pp. 2293–2298.
- ⁷J. Meier, U. Kroll, E. Vallat-Sauvain, J. Spitznagel, U. Graf, and A. Shah, “Amorphous solar cells, the micromorph concept and the role of VHF-GD deposition technique,” *Sol. Energy* **77**, 983–993 (2004).
- ⁸R. Collins, A. Ferlauto, G. Ferreira, C. Chen, J. Koh, R. Koval, Y. Lee, J. Pearce, and C. Wronski, “Evolution of microstructure and phase in amorphous, protocrystalline, and microcrystalline silicon studied by real time spectroscopic ellipsometry,” *Sol. Energy Mater. Sol. Cells* **78**, 143–180 (2003).
- ⁹B. Yan, J. Yang, and S. Guha, “Effect of hydrogen dilution on the open-circuit voltage of hydrogenated amorphous silicon solar cells,” *Appl. Phys. Lett.* **83**, 782–784 (2003).
- ¹⁰R. Schropp, J. Rath, and H. Li, “Growth mechanism of nanocrystalline silicon at the phase transition and its application in thin film solar cells,” *J. Cryst. Growth* **311**, 760–764 (2009).
- ¹¹P. Roca i Cabarrocas, A. Fontcuberta i Morral, and Y. Poissant, “Growth and optoelectronic properties of polymorphous silicon thin films,” *Thin Solid Films* **403–404**, 39–46 (2002).
- ¹²A. Fontcuberta i Morral and P. Roca i Cabarrocas, “Structure and hydrogen content of polymorphous silicon thin films studied by spectroscopic ellipsometry and nuclear measurements,” *Phys. Rev. B* **69**, 125307 (2004).
- ¹³B. Rech, T. Roschek, J. Müller, S. Wieder, and H. Wagner, “Amorphous and microcrystalline silicon solar cells prepared at high deposition rates using RF (13.56 MHz) plasma excitation frequencies,” *Sol. Energy Mater. Sol. Cells* **66**, 267–273 (2001).
- ¹⁴M. Fischer, R. J. V. Quax, M. Zeman, and A. H. M. Smets, “Degradation kinetics of amorphous silicon solar cells processed at high pressure and its relation to the nanostructure,” *IEEE Photovoltaic Specialists Conference Proceedings*, Tampa, FL, 2013.
- ¹⁵A. Matsuda, “Thin-film silicon—growth process and solar cell application,” *Jpn. J. Appl. Phys., Part 1* **43**, 7909–7920 (2004).
- ¹⁶S. Shimizu, M. Kondo, and A. Matsuda, “A highly stabilized hydrogenated amorphous silicon film having very low hydrogen concentration and an improved Si bond network,” *J. Appl. Phys.* **97**, 033522 (2005).
- ¹⁷T. Moustakas and R. Friedman, “Amorphous silicon p-i-n solar cells fabricated by reactive sputtering,” *Appl. Phys. Lett.* **40**, 515–517 (1982).
- ¹⁸B. Schroeder, U. Weber, H. Seitz, A. Ledermann, and C. Mukherjee, “Current status of the thermo-catalytic (hot-wire) CVD of thin silicon films for photovoltaic applications,” *Thin Solid Films* **395**, 298–304 (2001).
- ¹⁹S. Filonovich, P. Alpuim, L. Rebouta, J.-E. Bourée, and Y. Soro, “Hydrogenated amorphous and nanocrystalline silicon solar cells deposited by HWCVD and RF-PECVD on plastic substrates at 150 °C,” *J. Non-Cryst. Solids* **354**, 2376–2380 (2008).
- ²⁰B. Korevaar, A. Petit, C. Smit, R. van Swaaij, and M. van de Sanden, “Effect of buffer layers on p-i-n a-Si:H solar cells deposited at high rate utilising an expanding thermal plasma,” in *IEEE Photovoltaic Specialists Conference*, New Orleans, LA (IEEE, 2002), pp. 1230–1233.
- ²¹See <http://www.indeotec.com> for more information about INDEOtec SA (Switzerland).
- ²²A. Howling, B. Strahm, P. Colsters, L. Sansonnens, and C. Hollenstein, “Fast equilibration of silane/hydrogen plasmas in large area RF capacitive reactors monitored by optical emission spectroscopy,” *Plasma Sources Sci. Technol.* **16**, 679–696 (2007).
- ²³M. Python, E. Vallat-Sauvain, J. Bailat, D. Domin, L. Fesquet, A. Shah, and C. Ballif, “Relation between substrate surface morphology and microcrystalline silicon solar cell performance,” *J. Non-Crystal. Solids* **354**, 2258–2262 (2008).
- ²⁴S. Nicolay, M. Benkhaira, L. Ding, J. Escarre, G. Bugnon, F. Meillaud, and C. Ballif, “Control of CVD-deposited ZnO films properties through water/DEZ ratio: Decoupling of electrode morphology and electrical characteristics,” *Sol. Energy Mater. Sol. Cells* **105**, 46–52 (2012).
- ²⁵L. Fanni, L. Ding, M. Benkhaira, M. Morales Masis, S. Nicolay, and C. Ballif, “Switching from a- to c-axis MOCVD ZnO films: On the morphological, optical and electrical changes” (unpublished).
- ²⁶P. Cuony, M. Marending, D. Alexander, M. Boccard, G. Bugnon, M. Despeisse, and C. Ballif, “Mixed-phase p-type silicon oxide containing silicon nanocrystals and its role in thin-film silicon solar cells,” *Appl. Phys. Lett.* **97**, 213502 (2010).
- ²⁷M. Despeisse, G. Bugnon, A. Feltrin, M. Stueckelberger, P. Cuony, F. Meillaud, A. Billet, and C. Ballif, “Resistive interlayer for improved performance of thin film silicon solar cells on highly textured substrate,” *Appl. Phys. Lett.* **96**, 073507 (2010).
- ²⁸IEC (International Electrotechnical Commission), “IEC 60904-9 Ed.2: Photovoltaic devices—Part 9: Solar simulator performance requirements” (2007).
- ²⁹IEC (International Electrotechnical Commission), “IEC 60904-3 Ed.2: Photovoltaic devices—Part 3: Measurement principles for terrestrial photovoltaic (PV) solar devices with reference spectral irradiance data” (2006).
- ³⁰IEC (International Electrotechnical Commission), “IEC 61646 Ed.2: Thin-film terrestrial photovoltaic (PV) modules—Design qualification and type approval” (2008).
- ³¹M. Lieberman and A. Lichtenberg, *Principles of Plasma Discharges and Materials Processing* (John Wiley & Sons, Inc., 2005).
- ³²V. Lisovskiy and V. Yegorenkov, “Rf breakdown of low-pressure gas and a novel method for determination of electron-drift velocities in gases,” *J. Phys. D: Appl. Phys.* **31**, 3349–3357 (1998).
- ³³T. Kihara, “The mathematical theory of electrical discharges in gases,” *Rev. Mod. Phys.* **24**, 45–61 (1952).
- ³⁴V. Lisovskiy, J.-P. Booth, K. Landry, D. Douai, V. Cassagne, and V. Yegorenkov, “Similarity law for rf breakdown,” *Europhys. Lett.* **82**, 15001 (2008).
- ³⁵V. Lisovskiy, J.-P. Booth, K. Landry, D. Douai, V. Cassagne, and V. Yegorenkov, “Electron drift velocity in argon, nitrogen, hydrogen, oxygen and ammonia in strong electric fields determined from rf breakdown curves,” *J. Phys. D: Appl. Phys.* **39**, 660–665 (2006).
- ³⁶V. Lisovskiy, J.-P. Booth, K. Landry, D. Douai, V. Cassagne, and V. Yegorenkov, “Electron drift velocity in silane in strong electric fields determined from rf breakdown curves,” *J. Phys. D: Appl. Phys.* **40**, 3408–3410 (2007).
- ³⁷B. Strahm, A. Howling, L. Sansonnens, and C. Hollenstein, “Plasma silane concentration as a determining factor for the transition from amorphous to microcrystalline silicon in SiH₄/H₂ discharges,” *Plasma Sources Sci. Technol.* **16**, 80–89 (2007).
- ³⁸C. Niikura, N. Itagaki, and A. Matsuda, “Guiding principles for obtaining high-quality microcrystalline silicon at high growth rates using SiH₄/H₂ glow-discharge plasma,” *Jpn. J. Appl. Phys., Part 1* **46**, 3052–3058 (2007).

- ³⁹M. Tsuda, S. Oikawa, and K. Sato, "On the primary process in the plasma-chemical and photochemical vapor deposition from silane. III. Mechanism of the radiative species Si(1P0) formation," *J. Chem. Phys.* **91**, 6822–6829 (1989).
- ⁴⁰J. Perrin, "Modelling of the power dissipation and rovibrational heating and cooling in SiH₄-H₂ RF glow discharges," *J. Phys. D: Appl. Phys.* **26**, 1662–1679 (1993).
- ⁴¹J. Andújar, E. Bertran, A. Canillas, J. Campmany, and J. Morenza, "Effect of substrate temperature on deposition rate of rf plasma-deposited hydrogenated amorphous silicon thin films," *J. Appl. Phys.* **69**, 3757–3759 (1991).
- ⁴²A. Matsuda, "Formation kinetics and control of microcrystallite in $\mu\text{-Si:H}$ from glow discharge plasma," *J. Non-Crystal. Solids* **59–60**, 767–774 (1983).
- ⁴³J. Dorier, C. Hollenstein, A. Howling, and U. Kroll, "Powder dynamics in very high frequency silane plasmas," *J. Vac. Sci. Technol. A* **10**, 1048–1052 (1992).
- ⁴⁴G. Jellison and F. Modine, "Parameterization of the optical functions of amorphous materials in the interband region," *Appl. Phys. Lett.* **69**, 371 (1996).
- ⁴⁵B. Kalache, A. Kosarev, R. Vanderhaghen, and P. Roca i Cabarrocas, "Ion bombardment effects on microcrystalline silicon growth mechanisms and on the film properties," *J. Appl. Phys.* **93**, 1262–1273 (2003).
- ⁴⁶B. von Roedern, L. Ley, and M. Cardona, "Photoelectron spectra of hydrogenated amorphous silicon," *Phys. Rev. Lett.* **39**, 1576–1580 (1977).
- ⁴⁷G. Cody, T. Tiedje, B. Abeles, B. Brooks, and Y. Goldstein, "Disorder and the optical-absorption edge of hydrogenated amorphous silicon," *Phys. Rev. Lett.* **47**, 1480–1483 (1981).
- ⁴⁸A. Smets, M. Wank, B. Vet, M. Fischer, R. van Swaaij, M. Zeman, D. Bobela, C. Wronski, and R. van de Sanden, "The relation between the bandgap and the anisotropic nature of hydrogenated amorphous silicon," *IEEE J. Photovoltaics* **2**, 94–98 (2012).
- ⁴⁹M. Fecioru-Morariu, B. Mereu, J. Kalas, J. Hoetzel, P. A. Losio, M. Kupich, O. Kluth, and T. Eisenhammer, "High quality amorphous silicon layers for large area thin film PV applications," in *25th EU PVSEC/WCPEC-5 Proceedings*, Valencia, Spain (WIP Wirtschaft und Infrastruktur GmbH & Co Planungs-KG, 2010), pp. 2947–2950.
- ⁵⁰P. Alpuim, V. Chu, and J. Conde, "Amorphous and microcrystalline silicon films grown at low temperatures by radio-frequency and hot-wire chemical vapor deposition," *J. Appl. Phys.* **86**, 3812–3821 (1999).
- ⁵¹A. H. M. Smets and M. C. M. van de Sanden, "Relation of the Si-H stretching frequency to the nanostructural Si-H bulk environment," *Phys. Rev. B* **76**, 073202 (2007).